npj | Quantum Materials

www.nature.com/npjquantmats

ARTICLE OPEN

Check for updates

Large Zeeman splitting induced anomalous Hall effect in $ZrTe_5$

Zeliang Sun[1], Zhipeng Cao[2,3], Jianhua Cui[1], Changsheng Zhu[1], Donghui Ma[1], Honghui Wang[1], Weizhuang Zhuo[1], Zhaohui Cheng[1], Zhenyu Wang[1], Xiangang Wan[2,3]✉ and Xianhui Chen[1,2,4]✉

Berry phase effects have significant influences on the electronic properties of condensed matter. In particular, the anomalous Hall conductivity has been recognized as an intrinsic property of the systems with non-zero Berry curvature. Here, we present the anomalous Hall effect observed in the non-magnetic material $ZrTe_5$, which hosts a large Zeeman splitting with Landé *g*-factor of 26.49. The quantum oscillation analysis reveals non-linear band dispersion near the top of valence band in bulk band structure, and no Weyl node forms with applied magnetic field. The anomalous Hall conductivity reaches 129 Ω^{-1} cm^{-1} at 2 K, and shows weak temperature dependence. All these combined with theoretical analysis suggest that the anomalous Hall effect observed in $ZrTe_5$ originates from the non-vanishing Berry curvature induced by combining large Zeeman splitting and strong spin–orbit coupling. Remarkably, the anomalous Hall resistivity reverses its sign from negative to positive at a hydrostatic pressure $P = 1.3$ GPa, which confirms that the anomalous Hall effect in $ZrTe_5$ is highly related to the band structure-dependent Berry curvature. Our results have verified the anomalous Hall mechanism in $ZrTe_5$ and offer a new platform to study the anomalous Hall effect.

npj Quantum Materials (2020)5:36 ; https://doi.org/10.1038/s41535-020-0239-z

INTRODUCTION

The ordinary Hall effect arises from the Lorentz force bending of charge carriers' path under a magnetic field. On the other hand, the anomalous Hall effect (AHE) occurs due to the transverse velocity of carriers, which can be engendered by two classes of mechanisms[1,2]: the extrinsic mechanism owing to spin-dependent impurity scattering effects[3–5], including skew-scattering and side jump, and the intrinsic mechanism, which is related to the non-zero Berry curvature[1,2,6–9]. The intrinsic mechanism is only dependent on the band structure and it is proposed that the non-zero Berry curvature can generate an anomalous velocity in the direction transverse to the electric field and external magnetic field, which gives rise to an anomalous Hall current resulting in intrinsic contribution to the Hall conductivity[10–14]. Such intrinsic contribution dominates when the Fermi level is located around the band crossing point where the Berry curvature is significantly enhanced[8,9]. Magnetic Weyl semimetals with broken time-reversal symmetry (TRS) are expected to exhibit strong intrinsic AHE owing to their large Berry curvature around the Weyl points. Recently, large intrinsic AHE has been observed in magnetic kagome lattice[15–17] and Heusler[18–20] compounds with possible non-trivial band topology. In principle, broken TRS can give rise to non-zero anomalous Hall conductivity in the presence of strong spin–orbit coupling (SOC), whether Weyl points are present or not[1,6].

Here, we study the AHE in flux-grown non-magnetic single-crystal $ZrTe_5$ and we propose an alternative route to realize AHE in $ZrTe_5$, where the non-zero Berry curvature originates from the combination of large Zeeman splitting and strong SOC in our $ZrTe_5$ samples. Our samples show good crystalline quality, which enables the observation of quantum oscillations. By the analysis of quantum oscillation, we obtained non-linear band dispersion near the top of valence band in the bulk band structure and no Weyl node forms in our $ZrTe_5$ samples. We observed clear AHE that shows weak temperature dependence, indicating the anomalous Hall conductivity arises from intrinsic Berry curvature. Supported by theoretical analysis, it suggests the AHE in $ZrTe_5$ arises from the large Zeeman splitting in the presence of strong SOC, without the existence of Weyl nodes. Furthermore, the anomalous Hall resistivity reverses its sign at a hydrostatic pressure $P = 1.3$ GPa, which also corroborates that the AHE in $ZrTe_5$ arises from the band structure-dependent Berry curvature. Our work not only indicates the AHE observed in $ZrTe_5$ arises from the Berry curvature generated from combining large Zeeman splitting and strong SOC, but also provides a new insight into searching and studying the anomalous Hall effect in real materials.

RESULTS AND DISCUSSION

As depicted in Fig. 1a, the $ZrTe_3$ chains run along the *a*-axis and form a quasi-two-dimensional layer via linking zigzag chains of Te atoms along the *c*-axis. The quasi-two-dimensional layers stack along the *b*-axis crystalizing an orthorhombic structure with space group *Cmcm* (D_{2h}^{17}). Single layer $ZrTe_5$ is predicted to be a candidate for quantum spin Hall (QSH) insulator[21], whereas it is still under debate whether the bulk $ZrTe_5$ is weak topological insulator or three-dimensional Dirac semimetal[22–30]. Recently, unconventional physical phenomena that may be related to the Berry phase effects have been observed in this compound[30–33].

The magneto-transport properties of $ZrTe_5$ were measured with the current applied along *a*-axis and magnetic field applied along *b*-axis (see inset of Fig. 1c). Typical temperature-dependent

[1]Hefei National Laboratory for Physical Sciences at Microscale and Department of Physics, and Key Laboratory of Strongly-Couple Quantum Matter Physics, Chinese Academy of Sciences, University of Science and Technology of China, 230026 Hefei, Anhui, China. [2]Collaborative Innovation Center of Advanced Microstructures, Nanjing University, 210093 Nanjing, China. [3]National Laboratory of Solid State Microstructures and School of Physics, Nanjing University, 210093 Nanjing, China. [4]CAS Center for Excellence in Quantum Information and Quantum Physics, 230026 Hefei, Anhui, China. ✉email: xgwan@nju.edu.cn; chenxh@ustc.edu.cn

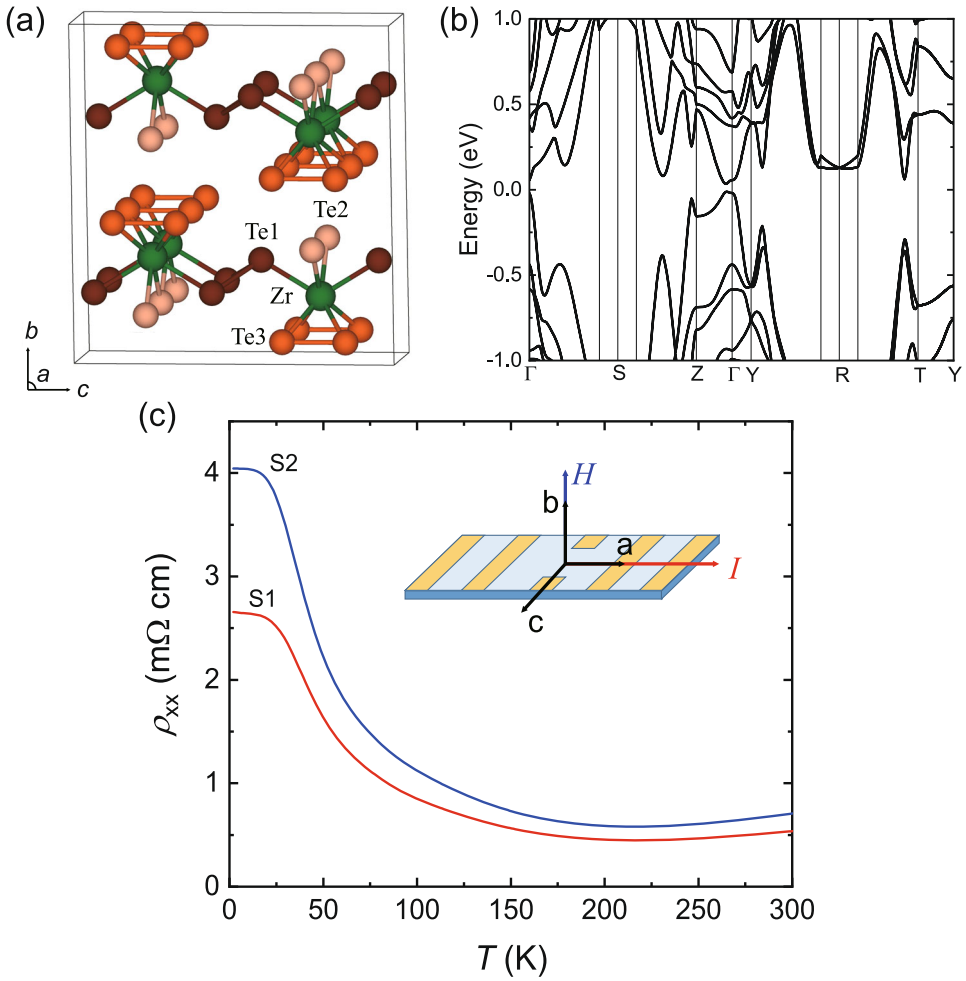

Fig. 1 Crystal and electronic structures of $ZrTe_5$ and the measured electric resistivity. a Crystal structure of $ZrTe_5$. **b** Band structure of $ZrTe_5$. **c** Temperature-dependent resistivity of $ZeTe_5$ with current along *a*-axis for samples S1, S2. The inset shows the schematic for electrical transport measurements.

resistivity curves of two $ZrTe_5$ samples are shown in Fig. 1c, labeled as S1 and S2, respectively. The resistivity ρ_{xx} first decreases with decreasing temperature and reaches a minimum at about 220 K, and then increases with further decreasing temperature down to 20 K, below which it tends to a saturation. We note that this resistivity behavior is different from that has been observed in chemical vapor transport (CVT)-grown $ZrTe_5$ showing a resistivity peak[25], but is similar to the resistivity curve reported in refs. [31,34,35]. We ascribe this absence of resistivity peak to the much smaller density of impurities and defects in our samples, since Te deficiency can be largely reduced in our samples by using the Te-flux method and the modified growth parameters. This results in a semiconducting-like behavior in the resistivity.

Our first task is to clarify the band-topological properties of our $ZrTe_5$ samples. The transverse magnetoresistance (MR) of sample S1 at various temperatures from 2 to 15 K is shown in Fig. 2a. It exhibits pronounced Shubnikov-de Haas (SdH) oscillations and reaches a non-saturated value of ~1200% at 9 T. By subtracting a smooth background, we obtained the oscillation patterns at different temperatures, as shown in Fig. 2b. Following the Lifshitz-Kosevich (LK) formula, the quantum oscillation of resistivity could be written as[36,37]

$$\Delta\rho \propto R_T R_D R_s \cos\left[2\pi\left(\frac{F}{H} - \gamma + \delta\right)\right] \quad (1)$$

where F is the oscillation frequency, R_T, R_D, and R_s are damping factors corresponding to temperature, scattering and spin splitting, respectively. γ is the Onsager phase factor and δ is an additional phase shift ranging from −1/8 to 1/8 depending on the degree of the dimensionality of the Fermi surface. Since in our $ZrTe_5$ samples, the value ρ_{xx}/ρ_{yx} is ~2.8–8.7 in the oscillation (see Supplementary Fig. 1), we have $\sigma_{xx} = \frac{\rho_{xx}}{\rho_{xx}^2+\rho_{yx}^2} \sim 1/\rho_{xx}$. Consequently, the oscillation of ρ_{xx} is totally out-of-phase with σ_{xx}, and we labeled the valleys of the oscillating pattern as the integer Landau indices. The Landau index n versus $1/\mu_0 H$ at 2 K are shown in Fig. 2c. The oscillation frequency F, determined by the slope in the linear fit of the index plots, is 4.36 T. According to the Onsager quantization rule, F is proportional to the extremal cross-sectional area S_F of the Fermi surface normal to the magnetic field, $F = (\hbar/2\pi e)S_F$. This yields a tiny cross-sectional area $S_F = 0.042\ \mathrm{nm}^{-2}$, manifesting that there is a quite small Fermi pocket. The extrapolation intercept gives $\gamma - \delta = 0.44 \pm 0.03$. The Onsager phase γ is defined as $\gamma = ½ - \phi_B/2\pi$, where ϕ_B is Berry phase. In an electron system that exhibits parabolic energy dispersion, ϕ_B is zero and $\gamma = 1/2$. Nevertheless, in a massless Dirac electron system with linear energy dispersion, a non-trivial Berry phase $\phi_B = \pi$ exists, which leads to a zero Onsager phase factor[38]. The extracted intercept of our $ZrTe_5$ sample indicates that the SdH effect comes from a non-linear dispersive band, which is in accordance with previous angle-resolved photoemission spectroscopy (ARPES) results[31] and our electronic band structure calculations (Fig. 1b), but in striking contrast to that previously found in CVT-grown

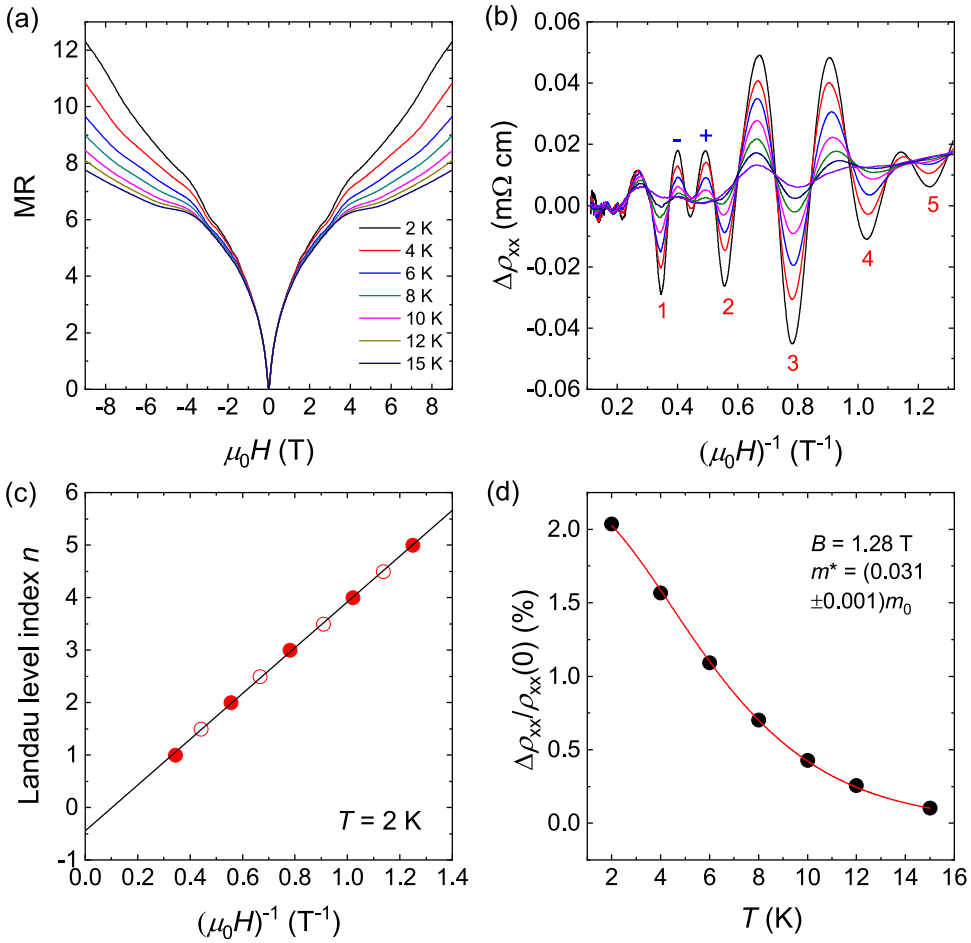

Fig. 2 Magnetoresistance of $ZrTe_5$. a Field dependence of MR at different temperatures with the magnetic field along *b*-axis and the current along *a*-axis. Prominent SdH oscillations show up at low temperatures. **b** Oscillatory component $\Delta\rho_{xx}$ as a function of inverse magnetic field taken at various temperatures. The valleys of the oscillating pattern are labeled as integer Landau indices. A large Zeeman splitting is observed between $n = 1$ and $n = 2$ Landau level. **c** Landau index n versus $1/\mu_0 H$ for the SdH oscillation. The non-zero intercept indicates trivial Berry phase in our $ZrTe_5$ samples. **d** Temperature dependence of the oscillation amplitude at 1.28 T.

$ZrTe_5$ (ref. [25]). This also excludes the emergence of Weyl nodes induced by Zeeman splitting in our $ZrTe_5$ samples[39].

By analyzing the temperature dependence of the oscillation amplitude based on the Lifshitz-Kosevich formula via $R_T = \frac{2\pi^2 k_B T/\hbar\omega_c}{\sinh(2\pi^2 k_B T/\hbar\omega_c)}$ (Fig. 2d), we got a tiny carrier cyclotron mass $m^* = (0.031 \pm 0.001)m_e$. Prominent spin splitting exists between $n = 2$ and $n = 1$ Landau level (Fig. 2b). We extracted the spin-splitting parameter $S = (1/2)g(m^*/m_e) = F\Delta(1/H)$ from the oscillation curves, where $\Delta(1/H)$ is the spacing between the split peaks corresponding to the up and down spins on one Landau level. We obtained a large Landé *g*-factor with the value of 26.49 in our samples, which is slightly larger than the result in previous report[25,40]. This large Landé *g*-factor indicates that there is strong SOC in $ZrTe_5$ and large energy splitting of electronic band can occur once external magnetic field is applied.

The Hall resistivity $\rho_{yx}(H)$ of sample S1 at 2 K is displayed in Fig. 3a. A typical anomalous Hall feature is observed, which is similar to that in previous report[31]. In the presence of AHE, the total Hall resistivity is composed of two components[1,2]

$$\rho_{yx}^{tot} = \rho_{yx}^{O} + \rho_{yx}^{A} \quad (2)$$

where ρ_{yx}^{O} is the ordinary Hall resistivity that equals to $R_H B$, and ρ_{yx}^{A} is the anomalous Hall resistivity. From the linear fitting of the high-field ordinary Hall resistivity, we obtained a hole carrier density $n_h = 2.68 \times 10^{18}$ cm^{-3}. Such low hole density is consistent with the small hole Fermi pocket revealed by our quantum oscillation analysis and band structure calculation. The anomalous Hall component ρ_{yx}^{A} (inset of Fig. 3a) was extracted by subtracting ρ_{yx}^{O} from the raw data. The Hall resistivity of $ZrTe_5$ at different temperatures is displayed in Fig. 3b. Clear AHE signal sticks to 50 K. When $T > 50$ K, a Hall resistivity peak appears at low field in the $\rho_{yx}(H)$ curves (see Supplementary Fig. 2), indicating the coexistence of both hole carriers and electron carriers above 50 K[34,35]. This peak broadens with increasing temperature, and the $\rho_{yx}(H)$ curves becomes almost linear when $T > 160$ K, implying that the hole carriers dominate at high temperature.

Since $ZrTe_5$ is a non-magnetic material, the AHE we observed is not associated with spontaneous magnetization, or the topological Hall effect contributed to the non-zero spin chirality[1,2,41]. Further, the anomalous Hall conductivity $|\sigma_H^A|$ at 2 K is 129 Ω^{-1} cm^{-1} under 5 T, which is much larger than the anomalous Hall conductivity originated from the extrinsic mechanism in the bad metal hopping regime (typically 0.01 ~ 1 Ω^{-1} cm^{-1})[1,2,42]. As displayed in Fig. 3c, the anomalous Hall conductivity $|\sigma_H^A|$ shows quite weak temperature dependence, as expected for the intrinsic AHE. All these observations suggest that the AHE in $ZrTe_5$ arises from the intrinsic Berry curvature. Usually, the large Berry curvature is related to the Weyl nodes and intrinsic AHE has been observed in systems with magnetic Weyl fermions, where the non-zero Berry curvature is

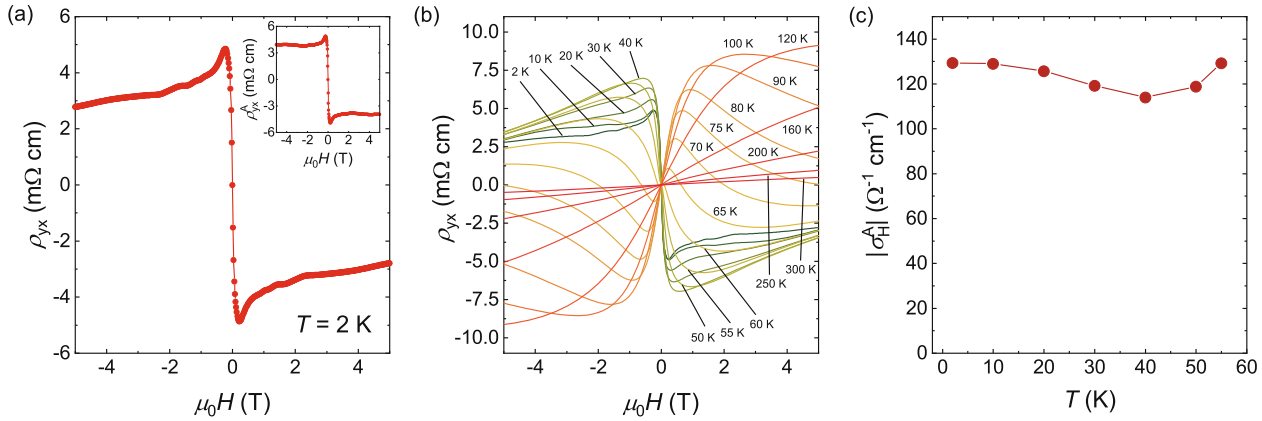

Fig. 3 Hall signals in $ZrTe_5$. a Hall resistivity of $ZrTe_5$ at 2 K with *H* along *b*-axis and *I* along *a*-axis. The inset shows anomalous component ρ_{yx}^{A} by subtracting normal Hall resistivity. **b** The Hall resistivity of $ZrTe_5$ at various temperatures. **c** The anomalous Hall conductivity $|\sigma_H^A|$ under 5 T at different temperatures.

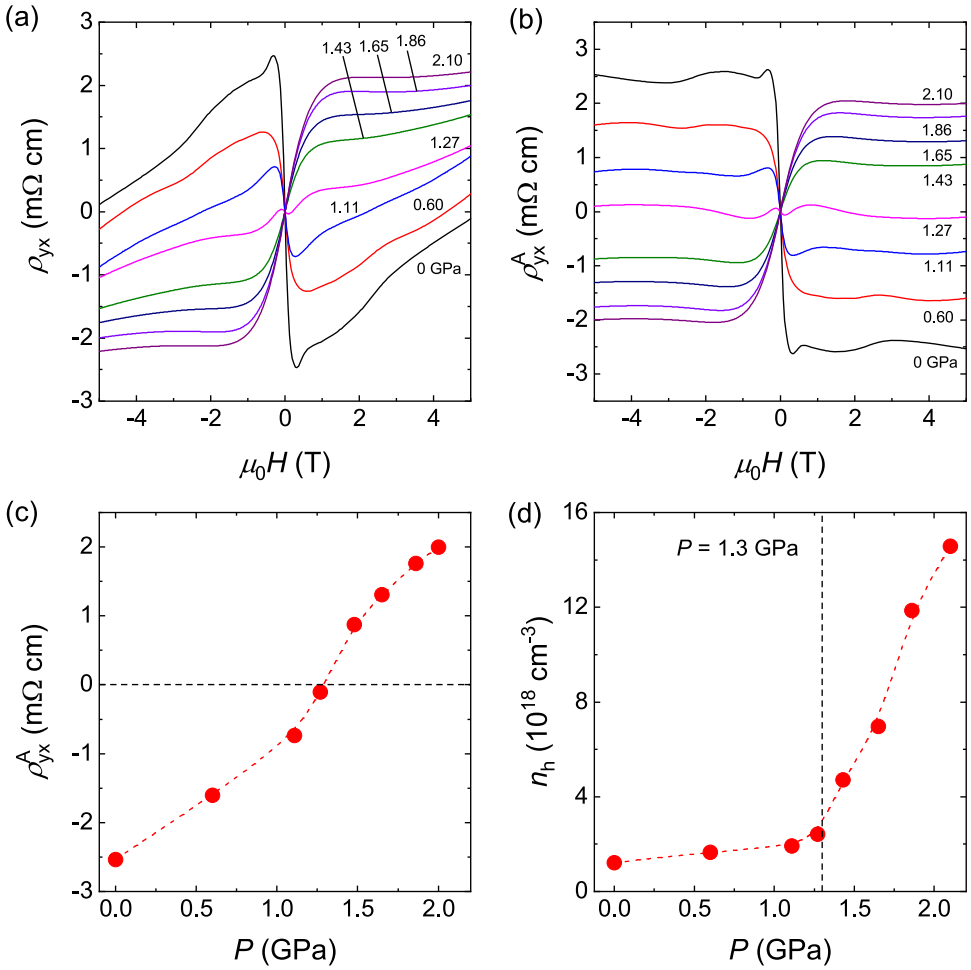

Fig. 4 Pressure-dependent anomalous Hall resistivity of $ZrTe_5$. a The Hall resistivity ρ_{yx} at 2 K under different pressures. **b** The anomalous component ρ_{yx}^{A} at various pressures. **c** Pressure dependence of anomalous Hall resistivity ρ_{yx}^{A}. It reverses sign from negative to positive at $P =$ 1.3 GPa. **d** Pressure-dependent hole carrier density. It increases with pressure and changes its slope at the sign-reversal pressure $P = 1.3$ GPa.

generated by the Weyl nodes[15–20]. However, there is no Weyl node appearing in our $ZrTe_5$ sample at zero or non-zero magnetic field. First, as $ZrTe_5$ is non-magnetic centrosymmetric material, Weyl nodes cannot exist at zero magnetic field. Second, quantum oscillation analysis and band structure calculation reveal non-linear band dispersion near the top of valence band and there is no Dirac node in our $ZrTe_5$ samples. This is also supported by previous ARPES data, which shows a hole Fermi pocket and non-linear band

dispersion in similar $ZrTe_5$ samples[31]. Thus, the Weyl nodes arising from splitting Dirac nodes under magnetic field cannot exist either. Third, the topologically trivial Berry phase revealed by the quantum oscillation analysis also suggests that no Zeeman splitting-induced Weyl nodes form under external magnetic field in our samples. Moreover, we can estimate the Zeeman energy to be 7.7 meV at 5 T using *g*-factor ~26.49, which is much smaller than the band gap of 46 meV from the band structure calculation. Previous ARPES and scanning tunneling microscopy (STM) results[22–24,43] reported a 20–100 meV band gap in $ZrTe_5$, which is in accordance with our theoretical calculation and larger than the estimated Zeeman energy ~7.7 meV. Magneto-spectroscopy measurement also reported a Dirac mass term, corresponding to a 10 meV band gap in the $ZrTe_5$ thin flake[40], which is also larger than our estimated Zeeman energy. These results indicate that the Zeeman splitting cannot induce band crossing and generate Weyl nodes in our $ZrTe_5$ samples. Given all above, there is no Weyl nodes formed at zero or non-zero magnetic field and the non-zero Berry curvature does not generate from Weyl nodes in our $ZrTe_5$ samples.

Theoretically, non-zero Berry curvature can be generated by combining large Zeeman splitting and strong spin–orbit coupling (SOC), regardless of whether Weyl node exists or not[1,6]. In non-magnetic centrosymmetric systems, such as $ZrTe_5$, the Berry curvature vanishes identically throughout the Brillouin zone from symmetry consideration when TRS preserves. Once magnetic field is applied, TRS is broken and Zeeman effect splits the doubly degenerate energy band into two separate ones. The spin–orbit interaction couples the spin-up and spin-down bands together, and transfers the time-reversal violation from spin degree of freedom to the orbital motion, giving rise to a non-zero Berry curvature[6]. This Berry curvature could be very large in materials with large spin–orbital coupling, such as $ZrTe_5$. In general, the anomalous Hall conductivity can be expressed by the integral of Berry curvature over the Brillouin zone as[1]:

$$\sigma_{ac} = \frac{e^2}{\hbar}\sum_n \int_{BZ} \frac{d^3k}{(2\pi)^3} f(\varepsilon_n(k))\Omega_{n,b}(k) \quad (3)$$

where σ_{ac} represents the in-plane anomalous Hall conductivity with magnetic field applied along *b*-axis, $f(\varepsilon_n(k))$ is the Fermi-Dirac distribution and $\Omega_{n,b}(k)$ is the Berry curvature of the *n*-th band along *b*-axis. Therefore, when external magnetic field set in, TRS is broken and the combination of large Zeeman splitting and strong SOC gives rise to a non-zero Berry curvature, which leads to the anomalous Hall conductivity in $ZrTe_5$.

To further investigate the AHE in $ZrTe_5$, we have performed detailed measurements under hydrostatic pressure on sample S2. Previous works have reported pressure can largely tune the structure of $ZrTe_5$ and induce topological phase transition and superconductivity in $ZrTe_5$ samples with resistivity peak[44,45]. Since the Berry curvature is only related to the electronic structure, the AHE should respond dramatically to the external pressure in $ZrTe_5$ in which the band structure is very sensitive to the changes in lattice parameters[21]. Figure 4a shows the pressure-dependent Hall resistivity ρ_{yx} of S2 at 2 K and the anomalous Hall resistivity component at various pressures is shown in Fig. 4b. Figure 4c displays the pressure dependence of anomalous Hall resistivity ρ_{yx}^{A}. The applied pressure reduces the negative anomalous Hall resistivity and the sign of the AHE changes from negative to positive at $P = 1.3$ GPa. Above this pressure, the positive anomalous Hall resistivity increases gradually.

The anomalous Hall conductivity arising from Berry curvature is sensitive to the Fermi level shift around the band crossing point[13]. The sign change behavior of AHE has been observed experimentally when the Fermi level passes though the band crossing point by controlling doping or temperature[9,46–48]. Nevertheless, we have demonstrated that there is no band crossing induced by Zeeman splitting in $ZrTe_5$ at ambient pressure. The hole carrier density increases continuously with pressure and carrier-type does not change (Fig. 4d). These suggest that the sign reversal of AHE does not originate from the Fermi level scanning through the band crossing point. Instead, since bulk $ZrTe_5$ is theoretically proposed to locate in the vicinity of a transition from strong topological insulator to weak topological insulator[21], the pressure-tuned band structure may lead to a significant change of the total Berry curvature, which can result in the sign reversal of AHE. Moreover, the pressure dependence of carrier density changes its slope at $P = 1.3$ GPa, implying that the Berry curvature of the occupied band has a drastic change around the sign-reversal pressure. To elucidate the sign-reversal behavior of AHE, we calculated the band structure of $ZrTe_5$ under different pressures, as shown in Supplementary Fig. 3. With increasing pressure, the valence band at Γ point moves downward gradually and a hole Fermi pocket emerges near *Z* point at about 1.3 GPa. Consequently, it implies that the Fermi pocket near *Z* point makes an inverse contribution to the total Berry curvature and it dominates above 1.3 GPa, resulting in the sign reversal of AHE. In addition, our numerical calculated results indicate that $ZrTe_5$ is in the strong topological insulator phase between 0 and 9 GPa. However, the topological characteristic of bulk $ZrTe_5$ is still controversial[22–30] and we can only exclude Weyl nodes in our samples, but cannot confirm the topological phase of $ZrTe_5$ based on our experiments.

In summary, we have studied the AHE in $ZrTe_5$ with non-linear band dispersion near the top of valence band, and verified that it originates from the combination of large Zeeman splitting and strong SOC, without the emergence of Weyl nodes. Our results reveal that $ZrTe_5$, owing to its simple electronic structure near the Fermi level, is a perfect candidate for investigating the AHE in non-magnetic system. Moreover, the continuous control of AHE in $ZrTe_5$ under hydrostatic pressure provides an ideal platform for exploring how the Berry curvature is affected by the detailed electronic structures.

METHODS

Single-crystal growth

The single crystals of $ZrTe_5$ in our studies were grown using the Te-flux method. Zr slug and Te shots in an atomic ratio of 1:49 were loaded into a canfield crucible set, then sealed into a silica ampoule under vacuum. The ampoule was heated to 1000 °C and kept for 12 h to homogenize the melt. It was cooled down to 650 °C rapidly, and then cooled to 460 °C in 60 h. $ZrTe_5$ crystals were isolated from Te flux by centrifuging at 460 °C.

Transport measurement

The samples are needlelike shape with typical dimensions of $1.8 \times 0.08 \times 0.03$ mm. The electrical contacts were arranged in a conventional Hall-bar configuration with the current along *a*-axis and magnetic field along *b*-axis. To have a good contact, we first deposited 100 nm Au on the electrode pattern and then contacted the electrical leads with platinum wires by silver paint. The magneto-transport measurements were performed in a Quantum Design PPMS-9T system. Hydrostatic pressure was established in Quantum Design high-pressure piston-cylinder cell with Daphne 7373 oil used as pressure transmitting medium. Pressure was calibrated by measuring the superconducting transition temperature of pure tin with an uncertainty of 0.02 GPa.

Density functional theory (DFT) calculations

The first-principles calculations based on the density functional theory (DFT) were implemented in Vienna ab-initio Simulation Package (VASP) code[49,50]. The Perdew–Burke–Ernzerhof (PBE) functional of generalized gradient approximation (GGA)[51,52] was employed as the exchange-correlation potential, and the projector augmented wave (PAW) method[53] was chosen to treat core-valence electron interactions. The plane wave cutoff energy was 460 eV, with the Brillouin zone sampled by a $12 \times 12 \times 7$ mesh. Spin–orbit coupled (SOC) effect was taken into account in all calculations.

DATA AVAILABILITY

The data that support the findings of this study are available from the corresponding author upon reasonable request.

CODE AVAILABILITY

The computer codes used to carry out the DFT calculations used in this work are available from the corresponding author upon reasonable request.

Received: 10 January 2020; Accepted: 7 May 2020;
Published online: 02 June 2020

REFERENCES

1. Nagaosa, N. et al. Anomalous Hall effect. *Rev. Mod. Phys.* **82**, 1539–1592 (2010).
2. Nagaosa, N. Anomalous Hall effect-A new perspective-. *J. Phys. Soc. Jpn.* **75**, 042001 (2006).
3. Smit, J. The spontaneous Hall effect in ferromagnetics I. *Physica* **21**, 877–887 (1955).
4. Smit, J. The spontaneous Hall effect in ferromagnetics II. *Physica* **24**, 39–51 (1958).
5. Berger, L. Side-jump mechanism for the Hall effect of ferromagnets. *Phys. Rev. B* **2**, 4559–4566 (1970).
6. Xiao, D., Chang, M. C. & Niu, Q. Berry phase effects on electronic properties. *Rev. Mod. Phys.* **82**, 1959–2007 (2010).
7. Haldane, F. D. M. Berry curvature on the Fermi surface: Anomalous Hall effect as a topological Fermi-liquid property. *Phys. Rev. Lett.* **93**, 206602 (2004).
8. Taguchi, Y. et al. Spin chirality, Berry phase, and anomalous Hall effect in a frustrated ferromagnet. *Science* **291**, 2573–2576 (2001).
9. Fang, Z. et al. The anomalous Hall effect and magnetic monopoles in momentum space. *Science* **302**, 92–95 (2003).
10. Chang, M. & Niu, Q. Berry phase, hyperorbits, and the Hofstadter spectrum: semiclassical dynamics in magnetic Bloch bands. *Phys. Rev. B* **53**, 7010–7023 (1996).
11. Chen, H., Niu, Q. & MacDonald, A. H. Anomalous Hall effect arising from noncollinear antiferromagnetism. *Phys. Rev. Lett.* **112**, 017205 (2014).
12. Jungwirth, T., Niu, Q. & MacDonald, A. H. Anomalous Hall effect in ferromagnetic semiconductors. *Phys. Rev. Lett.* **88**, 207208 (2002).
13. Onoda, M. & Nagaosa, N. Topological nature of anomalous Hall effect in ferromagnets. *J. Phys. Soc. Jpn.* **71**, 19–22 (2002).
14. Wang, X., Vanderbilt, D., Yates, J. R. & Souza, I. Fermi-surface calculation of the anomalous Hall conductivity. *Phys. Rev. B* **76**, 195109 (2007).
15. Kuroda, K. et al. Evidence for magnetic Weyl fermions in a correlated metal. *Nat. Mat.* **16**, 1090–1095 (2017).
16. Ye, L. et al. Massive Dirac fermions in a ferromagnetic kagome metal. *Nature* **555**, 638–642 (2018).
17. Liu, E. et al. Giant anomalous Hall effect in a ferromagnetic kagome-lattice semimetal. *Nat. Phys.* **14**, 1125–1131 (2018).
18. Suzuki, T. et al. Large anomalous Hall effect in a half-Heusler antiferromagnet. *Nat. Phys.* **12**, 1119–1123 (2016).
19. Chandra, S. et al. Anomalous Hall effect in Weyl semimetal half-Heusler compounds RPtBi (R = Gd and Nd). *Proc. Natl Acad. Sci.* **115**, 9140–9144 (2018).
20. Belopolski, I. et al. Discovery of topological Weyl fermions lines and drumhead surface states in a room temperature magnet. *Science* **365**, 1278–1281 (2019).
21. Weng, H., Dai, X. & Fang, Z. Transition-metal pentatelluride $ZrTe_5$ and $HfTe_5$: a paradigm for large-gap quantum spin Hall insulators. *Phys. Rev. X* **4**, 011002 (2014).
22. Wu, R. et al. Evidence for topological edge states in a large energy gap near the step edges on the surface of $ZrTe_5$. *Phys. Rev. X* **6**, 021017 (2016).
23. Li, X. B. et al. Experimental observation of topological edge states at the surface step of the topological insulator $ZrTe_5$. *Phys. Rev. Lett.* **116**, 176803 (2016).
24. Zhang, Y. et al. Electronic evidence of temperature-induced Lifshitz transition and topological nature in $ZrTe_5$. *Nat. Commun.* **8**, 15512 (2017).
25. Liu, Y. W. et al. Zeeman splitting and dynamical mass generation in Dirac semimetal $ZrTe_5$. *Nat. Commun.* **7**, 12516 (2016).
26. Chen, R. Y. et al. Optical spectroscopy study of the three-dimensional Dirac semimetal $ZrTe_5$. *Phys. Rev. B* **92**, 075107 (2015).
27. Chen, R. Y. et al. Magnetoinfrared spectroscopy of Landau levels and Zeeman splitting of three-Dimensional massless Dirac Fermions in $ZrTe_5$. *Phys. Rev. Lett.* **115**, 176404 (2015).
28. Manzoni, G. et al. Evidence for a strong topological insulator phase in $ZrTe_5$. *Phys. Rev. Lett.* **117**, 237601 (2016).
29. Martino, G. et al. Two-Dimensional conical dispersion in $ZrTe_5$ evidenced by optical spectroscopy. *Phys. Rev. Lett.* **112**, 217402 (2019).
30. Li, Q. et al. Chiral magnetic effect in $ZrTe_5$. *Nat. Phys.* **12**, 550–554 (2016).
31. Liang, T. et al. Anomalous Hall effect in $ZrTe_5$. *Nat. Phys.* **14**, 451–455 (2018).
32. Li, P. et al. Giant planar Hall effect in the Dirac semimetal $ZrTe_5$-δ. *Phys. Rev. B* **98**, 121108 (2018).
33. Ge, J. et al. Unconventional Hall effect induced by Berry curvature. Preprint at https://arxiv.org/abs/1905.06040 (2019).
34. Shahi, P. et al. Bipolar conduction as the possible origin of the electronic transition in pentatellurides: metallic vs semiconducting behavior. *Phys. Rev. X* **8**, 021055 (2018).
35. Wang, H. et al. Discovery of log-periodic oscillations in ultraquantum topological materials. *Sci. Adv.* **4**, eaau5096 (2018).
36. Shoenberg, D. in *Metals* (Cambridge University Press, Cambridge, England, 1984).
37. Murakawa, H. et al. Detection of Berry's phase in a bulk Rashba semiconductor. *Science* **342**, 1490–1493 (2013).
38. Mikitik, G. P. & Sharlai, Y. V. Manifestation of Berry's phase in metal physics. *Phys. Rev. Lett.* **82**, 2147–2150 (1999).
39. Hirschberger, M. et al. The chiral anomaly and thermopower of Weyl fermions in the half-Heusler GdPtBi. *Nat. Mat.* **15**, 1161–1165 (2016).
40. Jiang, Y. et al. Landau-level spectroscopy of massive Dirac fermions in single-crystalline $ZrTe_5$ thin flake. *Phys. Rev. B* **96**, 041101 (2017).
41. Mühlbauer, S. et al. Skyrmion lattice in a chiral magnet. *Science* **323**, 915–919 (2009).
42. Fukumura, T. et al. A scaling relation of anomalous Hall effect in ferromagnetic semiconductors and metal. *Jpn. J. Appl. Phys.* **46**, 642–646 (2007).
43. Xiong, H. et al. Three-dimensional nature of the band structure of $ZrTe_5$ measured by high-momentum-resolution photoemission spectroscopy. *Phys. Rev. B* **95**, 195119 (2017).
44. Zhou, Y. H. et al. Pressure-induced superconductivity in a three-dimensional topological material $ZrTe_5$. *Proc. Natl Acad. Sci.* **113**, 2904–2909 (2016).
45. Zhang, J. L. et al. Disruption of the accidental Dirac semimetal state in $ZrTe_5$ under hydrostatic pressure. *Phys. Rev. Lett.* **118**, 206601 (2017).
46. Takahashi, K. S. et al. Control of the Anomalous Hall effect by doping in Eu1-xLaxTiO$_3$ thin film. *Phys. Rev. Lett.* **103**, 057204 (2009).
47. Lee, W. L. et al. Dissipationless anomalous Hall current in the ferromagnetic spinel $CuCr_2Se_4$-xBrx. *Science* **303**, 1647–1649 (2004).
48. Yasuda, K. et al. Geometric Hall effects in topological insulator heterostructures. *Nat. Phys.* **12**, 555–559 (2016).
49. Kresse, G. & Furthmüller, J. Efficient iterative schemes for ab initio total-energy calculations using a plane-wave basis set. *Phys. Rev. B* **54**, 11169–11186 (1996).
50. Kresse, G. & Joubert, D. From ultrasoft pseudopotentials to the projector augmented-wave method. *Phys. Rev. B* **59**, 1758–1775 (1999).
51. Perdew, J. P., Burke, K. & Ernzerhof, M. Generalized gradient approximation made simple. *Phys. Rev. Lett.* **77**, 3865–3868 (1996).
52. Perdew, J. P., Burke, K. & Ernzerhof, M. Reply. *Phys. Rev. Lett.* **80**, 891 (1998).
53. Blöchl, P. E. Projector augmented-wave method. *Phys. Rev. B* **50**, 17953–17979 (1994).

ACKNOWLEDGEMENTS

We thank Z.J. Xiang, T. Wu and J.J. Ying for helpful discussions. This work was supported by the National Natural Science Foundation of China (Grants No. 11888101 and No. 11534010), the National Key R&D Program of China (Grants No. 2016YFA0300201 and No. 2017YFA0303001), the Key Research Program of Frontier Sciences, CAS, China (Grant No. QYZDY-SSW-SLH021), the Strategic Priority Research Pro-gram (B) of the Chinese Academy of Sciences (Grant No. XDB25010100), Science Challenge Project (Grant No. TZ2016004), and Hefei Science Center CAS (Grant No. 2016HSC-IU001).

AUTHOR CONTRIBUTIONS

X.H.C. conceived the project and supervised the overall research. Z.L.S. and H.H.W. grew $ZrTe_5$ single crystal. Z.L.S. performed the magneto-transport measurements with assistance from J.H.C., C.S.Z., D.H.M., W.Z.Z., and Z.H.C. Z.L.S. analyzed the transport data. Z.P.C. and X.G.W. provided ab initial band structure calculations and theoretical explanation. Z.L.S, Z.Y.W., X.G.W., and X.H.C. wrote the paper and all authors commented on the manuscript.

COMPETING INTERESTS

The authors declare no competing interests.

ADDITIONAL INFORMATION

Supplementary information is available for this paper at https://doi.org/10.1038/s41535-020-0239-z.

Correspondence and requests for materials should be addressed to X.W. or X.C.

Reprints and permission information is available at http://www.nature.com/reprints

Publisher's note Springer Nature remains neutral with regard to jurisdictional claims in published maps and institutional affiliations.